Design and Development of the MIT Humanoid: A Dynamic and Robust Research Platform

Andrew SaLoutos[*,1], Elijah Stanger-Jones[*,1], Yanran Ding[1], Matthew Chignoli[1], and Sangbae Kim[1]

Abstract— **Enabling humanoid robots to achieve human-level athletic feats, such as running and jumping, is at the frontier of robotics research. To execute these behaviors, a robot platform must have high power density and robust mechanical and electrical systems. In this paper, we present the MIT Humanoid, a robust research platform that is designed to meet these requirements and be able to perform highly dynamic, parkour-style motions. The robot is just over 1 m tall and weighs approximately 24 kg, with 18 actuated degrees of freedom, each of which has a custom high-torque proprioceptive motor module. We also present initial hardware results from our new platform, demonstrating model-based controllers for pose control, walking, and jumping. The robot's high control bandwidth allows us to achieve stable pose control and walking, and the high power density allows the robot to achieve vertical jumps of roughly 30 cm, as measured by torso displacement.**

I. INTRODUCTION

Across industry and academia, interest in humanoid robots is perhaps at an all-time high. Companies see the potential of humanoid robots to be general purpose automation devices, while researchers are inspired by the challenge of controlling machines to go beyond human levels of agility and athleticism. In a world designed for humans but undergoing increasing automation, humanoid robots seem likely to become ubiquitous due to their human-like form factor.

Developing general humanoid robots, however, is not an easy task. Skills that people take for granted, like stepping with one foot to recover balance after a shove, are extremely difficult control problems. Also, the impacts from every step or bump, even just during walking, can rapidly cause physical breakdowns in hardware systems. Most existing humanoid robot platforms perform conservative and stable motions, as they are limited not only by the capabilities of their controllers, but even more so by the robustness of their mechanical design and the power of their actuation systems.

To achieve these athletic, dynamic tasks, such as running, jumping, and flipping, we need to design systems to be less conservative. This requires maximizing the performance of the mechanical and electrical systems and maintaining a tight integration between the development of hardware and controllers. The best example of this is shown in the videos of the Atlas robot from Boston Dynamics [1]. However, the work going into those videos is done behind closed doors, and thus the design and control details have not been published.

*Authors contributed equally to this work.

[1]Authors are with the Biomimetic Robotics Laboratory at the Department of Mechanical Engineering, Massachusetts Institute of Technology (MIT), Cambridge, MA, 02139, USA. Email: {saloutos, elijahsj, yanran, chignoli}@mit.edu
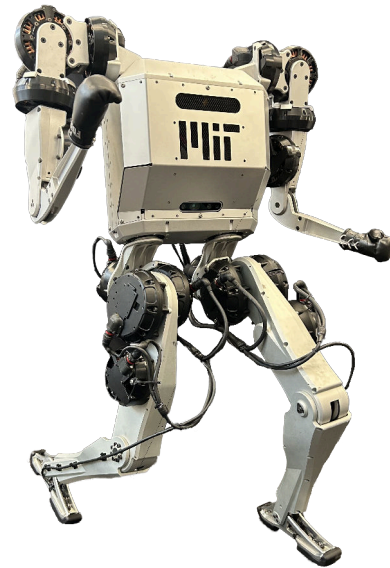

Fig. 1. **The MIT Humanoid.** The fully-assembled first version of the MIT Humanoid platform. The robot is 1.04 m tall and weighs approximately 24 kg. It has 18 total degrees of freedom: 5 per leg and 4 per arm. The core electronics and control computers are contained in the robot's torso.

In prior work, we demonstrated methods for control and planning through dynamic motions for a humanoid robot, but only in simulation [2]. Recently, we have designed and built a hardware platform capable of carrying out these motions, based on the design principles established in the Cheetah series of robots [3]–[5]. The robot, called the MIT Humanoid, is shown in Fig. 1. In this paper, we describe the robot's design, explain our key design decisions, and present preliminary hardware results.

II. BACKGROUND

There is a long history of interest in humanoid robots and bipedal locomotion, starting with the Raibert hoppers [6] developed in the 1980s. These were used for extracting useful first principles for dynamic legged locomotion that are still relevant to robot systems today. The ASIMO humanoid robot [7], unveiled in 2000, showcased impressively smooth and stable walking. This kickstarted development of other humanoid robot research platforms, such as the humanoid robots TORO [8], Lola [9], [10], and DRC-Hubo+ [11].

The arms and legs of these robots consist of serial chains of actuators. This results in heavy links and requires joint actuators capable of high continuous torques. To achieve the necessary joint torques, high gear reductions are used, but this comes at the cost of limiting joint speeds and greatly

increasing the reflected inertia of each joint. While these robots have enough degrees of freedom to complete complex tasks that combine locomotion and manipulation skills, their limited dynamic capabilities mean that they need to do so while perfectly statically stable. Any unexpected collision or disturbance can topple the robot faster than it can possibly react, since it has slow actuators and joints that are effectively rigid during impacts. Controllers must be designed with this in mind, which leads to conservative and brittle behaviors. However, the real world is dynamic and unpredictable, and tasks completion speed is often an important success metric, which limits the broader applicability of these types of humanoid robots.

To enhance impact robustness during locomotion, series-elastic actuators (SEAs) are commonly used. Notable examples include the bipedal robot ATRIAS [12] and its commercial successors, Cassie and Digit [13]. The recently developed humanoid robot JAXON3-P also uses this technology [14]. In SEAs, a spring element is placed in series with the motor. The spring absorbs impact forces, which protects the actuator's mechanical components, and the output torque can also be calculated by measuring the spring deflection. Using SEAs allows these robots to perform more dynamic locomotion, like jumping 0.3 m and landing [14] or running a 100 m race [15], since the repeated ground impacts will not cause excessive damage to the system. The downside of the SEAs, however, is that the series spring also limits the closed-loop control bandwidth of the actuator. So while the spring makes measuring the actuator torque, and thus performing torque control, possible, it also puts a lower ceiling on the dynamic motion capabilities of these robots.

Instead of electric motors, robots like Atlas [1] and Nadia [16] use hydraulic actuation. A key benefit of hydraulic actuation is that power can be allocated from the central power source to any joint, so that at any moment, a single joint can exert an extremely high instantaneous torque. This is especially useful for dynamic motions with high peak power requirements, like jumps and flips. However, designing and integrating high bandwidth valve controls and hydraulic channels and hoses, while keeping in mind the range-of-motion requirements of a robotic platform, requires tremendous engineering and maintenance efforts.

With the exception of Atlas, all of the humanoid or bipedal robots mentioned above struggle to emulate the dynamic motions of humans or even those of the one-legged Raibert hoppers. Quadruped robots, on the other hand, have been able to achieve much more impressive dynamic feats, such as backflips [5], [17], high-speed running [18], and jumping [19]. The success of dynamic locomotion for quadrupeds is due in part to four-legged locomotion being inherently more stable than bipedal locomotion. However, the most successful quadrupeds have also followed a different design paradigm [3], [4] than the humanoids and bipeds discussed previously. To achieve similar success for dynamic bipedal locomotion, we believe that we need to follow the same principles: designing humanoid robots with high torque density motors, low gear reductions, and low inertia limbs.
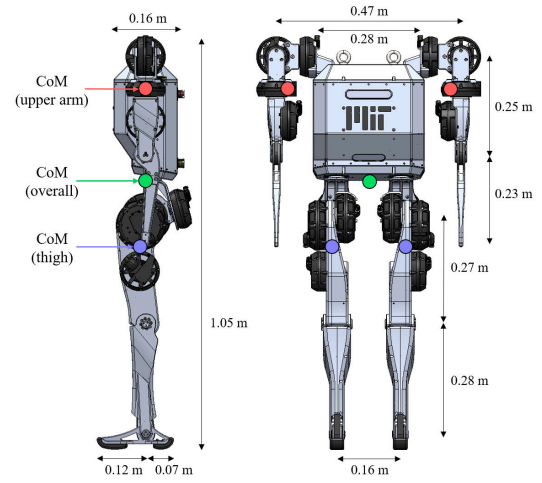

Fig. 2. **Key dimensions of the robot.** Key dimensions are labeled, including height, width, depth, and link lengths. Center of mass locations are shown for selected links and for the overall robot in this configuration.

This approach allows for improved impact robustness and higher force control bandwidth, both of which are necessary for dynamic behaviors, and are currently missing from most humanoid robot platforms.

Other recently introduced humanoid and biped designs have begun implementing these design principles. For example, the design of the leg of the Tello robot [20] and the PAL Kangaroo bipedal robot [21] both focus on moving actuators as close to the hip as possible. The humanoid robot Artemis [22] uses custom, large-diameter quasi-direct-drive motors in the legs, and also focuses on moving actuators up the legs, towards the torso. All three of these robots use linkages to drive the lower joints, which creates a non-linear relationship between force generation and torque from the motors and restricts the overall range of motion. These types of linkages are also typically quite fragile, making it difficult to sustain repeated impacts and unforeseen collisions.

We have developed the MIT Humanoid by following these same design principles, using custom modular actuators with high torque densities and minimizing limb inertias. With this robot, our design goal was not only to create a highly powerful, dynamic robotic system, but also a reliable and robust research platform.

III. DESIGN

The MIT Humanoid is designed to be capable of highly dynamic locomotion, while being robust to repeated impacts and disturbances. The robot is smaller than a full-sized human, but still roughly human-scale. This is intentional: we want our research findings to be relevant for surpassing human-level dynamic capabilities, but we also want the platform to be safe and easy to use for experiments.

The fully assembled robot is shown in Fig. 1 and CAD drawings with several key dimensions are shown in Fig. 2. The robot has four limbs, two arms and two legs, and is symmetric about the sagittal plane. It is 1.04 m tall and weighs approximately 24 kg. There are 18 total degrees of freedom, 5 per leg and 4 per arm. To minimize the limb
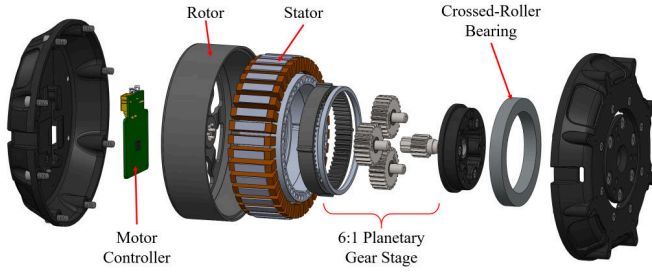
Fig. 3. **Exploded view of the U12 actuator.** The motor controller sits behind the rotor and stator, inside the rear housing. The planetary gear stage sits within the hollow stator. A crossed-roller bearing supports the planet carrier and the output face of the actuator. The U10 actuator is smaller, but has a similar internal design.
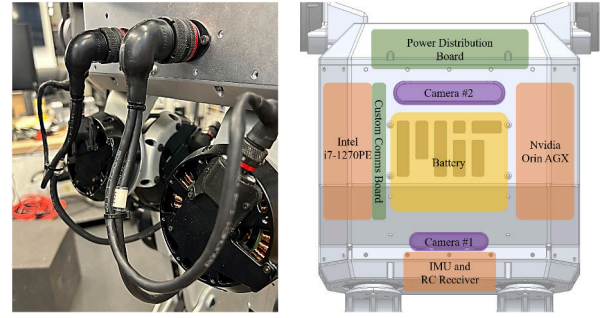

Fig. 4. **Control system components.** Left: One of the rugged cable harnesses for motor power and communication. Right: The contents of the robot torso include the two control computers, the power distribution board, the communication board, and the onboard sensors.

TABLE I

MODULAR ACTUATOR SPECIFICATIONS

Property	Actuator	
	U12	*U10*
Mass (g)	1100	660
Gear Ratio	6:1	6:1
Diameter × Thickness (mm)	126×46	101×38
Max. Torque (Nm)	72.0	34.0
Max. Speed at 60V (rad/s)	40.0	48.0
Rotor Inertia (kgm^2)	5.5e-4	1.7e-4

inertia, actuators were placed as close as possible to the torso, with belt transmissions for the knee, ankle, and elbow joints. The overall center of mass and the centers of mass of the arms and thigh links are also labeled in Fig. 2. All of the structural components are machined from 6061 or 7075 aluminum alloys, both of which are strong and lightweight.

Almost every component of the robot has been designed from scratch in the Biomimetic Robotics Lab, including the power distribution system, motor drivers and communication boards, along with the actuators and mechanical components. The computers and sensors are the only major components that are commercially available. This requires a large engineering effort, but the payoff is that the system is extremely well-understood and its performance can be optimized at every level, from motor driver firmware to actuator placement to high-level controllers.

A. Modular Actuators

The robot is designed around two types of modular actuators, which are summarized in Table I. Each actuator consists of a brushless DC motor with an integrated 6:1 planetary gear stage and a motor controller, inspired by the design of the MiniCheetah actuators [5]. They are built around frameless U12 and U10 motors from T-motor, with custom windings for improved torque density. Combined with the low gear ratio, this allows for high output torques and low reflected inertia. To reduce the structural weight and volume without sacrificing rigidity, we use crossed-roller bearings to support the output faces of the actuator gearboxes. The crossed-roller bearings are sized so that they can also support the links of the robot's limbs, reducing the necessary mechanical

structure and the total number of bearings. The geartrain is designed to withstand the maximum torque of the module. Since the modules are designed to have low reflected inertia, and the limbs are also designed to have low inertias, impact loading on the geartrain is not as severe. A labeled exploded view of the U12 actuator is shown in Fig. 3.

The integrated motor controllers accept bus voltages up to 60 V and can supply peak motor phase currents up to 60 A. Each controller has an STM32F446 microcontroller and a DRV8353 gate driver, along with a high-resolution iC-MU encoder that measures rotor position with 19 bits of resolution. This position signal is used for commutation and for tracking the output position of the actuator; there is no additional output position or torque sensing.

Inside of each actuator, the motor controller runs a local impedance control loop with a feed-forward torque term. The torque output of the impedance controller is converted to a desired motor current, which is then tracked using field-oriented control with a proportional-integral (PI) current controller. The local impedance control and current control loops both run at 20 kHz. For the impedance controller, the desired position, desired velocity, and feed-forward torque are updated via CAN commands at 1 kHz.

The 19-bit encoder resolution yields much cleaner velocity data, compared to standard 12-bit or 14-bit encoder resolutions. This allows us to greatly increase the local impedance control gains without causing instability, which directly improves the tracking performance for joint trajectories. Additionally, higher damping gains in the joint-level impedance controllers increase the overall system's stability, which allows for more aggressive feed-forward torque commands from high-level controllers.

Due to the low gear ratios of the actuators, using motor currents to control output torque is highly effective. Through careful testing with a custom dynamometer system [2], we are able to validate our torque control accuracy as well as generate motor efficiency maps, both of which are critical for understanding the high power capabilities of our system.

B. Computation, Communication, and Power Electronics

The torso of the robot, shown in the right side of Fig. 4, contains two computers as well as custom communications and power electronics components. The two computers serve

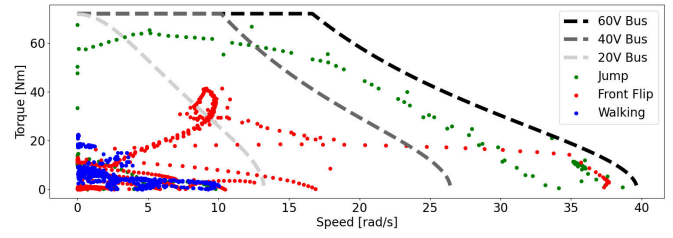| Joint	Name	Module	Max. Torque (Nm)	Max. Speed (rad/s)	Range of Motion [min, max] (deg)
q_1^l	Hip Yaw	U10	34.0	48.0	[-50, 70]
q_2^l	Hip Ab/Ad	U10	34.0	48.0	[-45, 60]
q_3^l	Hip Pitch	U12	72.0	40.0	[-55, 125]
q_4^l	Knee	U12	144.0	20.0	[-155, 5]
q_5^l	Ankle	U10	68.0	24.0	[-65, 55]
q_1^a	Shoulder Pitch	U10	34.0	48.0	[-180, 180]
q_2^a	Shoulder Roll	U10	34.0	48.0	[0, 180]
q_3^a	Shoulder Yaw	U10	34.0	48.0	[-180, 180]
q_4^a	Elbow	U10	51.0	32.0	[-145, 125]

Fig. 5. **Power requirements for U12 motor module.** The torque-speed curve for the U12 actuator is shown for three different bus voltages. Actuator states during three different simulated motions show that the 60 V bus voltage is necessary for dynamic behaviors.
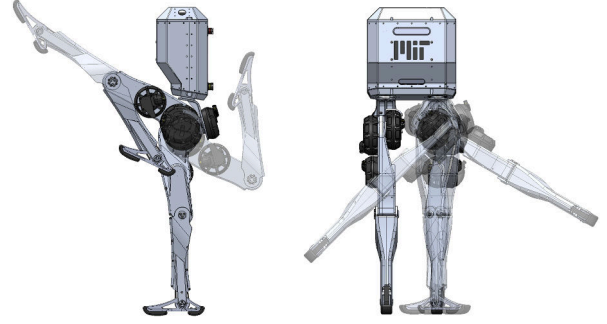

Fig. 6. **Range of motion of the left leg.** Left: Representative range of motion of hip pitch, knee, and ankle joints. Right: Representative range of motion of hip yaw and hip ab/ad joints. For clarity, the arms are not pictured.

different purposes: an Intel i7-1270PE is used for real-time processing and control, and an Nvidia Orin AGX is used for vision processing, data logging and other higher latency computation. To communicate with the motors and sensor suite, we use a custom communications platform with six CAN busses for high-frequency communication with the motors and auxiliary UART busses for communication with the other sensors located in the body. The torso also contains sensors, cameras, and a slot for a removable battery.

The robot is designed to be powered by a commercially available 60 V power-tool battery that has a capacity of 240 Wh. This would allow the robot to walk for around one hour. For the most dynamic behaviours achieved in simulation [2], we plan on developing a custom battery that can meet the high power requirements.

The 60 V bus voltage was chosen as it offers a balance between physical component sizing for the power electronics and power capabilities of the system. The package volume of the core power electronics components, such as MOSFETS and gate drivers, does not dramatically increase until 100 V, allowing the power electronics to be roughly the same physical volume as those of the MiniCheetah, which runs at a bus voltage of 20 V. To visualize the power requirements of the system, the torque-speed curves of the U12 motor module for different bus voltages are plotted in Fig. 5, along with data from a knee motor during three different motions. As the system bus voltage increases, the peak power capability increases. Fig. 5 shows that this additional power is critical for the dynamic behaviors we aim to achieve.

One of the key failure modes of robotic systems is the electrical cabling. So, to allow for highly dynamic motions without constant wiring failures, we use Deutsch AS ruggedized metal connectors for all of the exterior electrical connections. A picture of one of the harnesses is shown in the left of Fig. 4. The harness is designed to withstand snares and collisions without restricting the full range of motion of the robot joints.

C. Leg Design Details

Each leg has five degrees of freedom: three at the hip, one at the knee, and one at the ankle. For the knee and ankle joints, the actuators are located on the upper leg link and belts are used to drive the joints. The actuator types,

maximum speeds and torques, and ranges of motion for each joint are given in the top five rows of Table II. Fig. 6 shows several poses within the functional range of motion of the left leg. The joint and actuator axes, along with other design details, are depicted in the left of Fig. 7.

The total mass of each leg is 5.28 kg, or roughly 20% of the total robot mass. Of that, the actuators comprise 3.52 kg, while just 1.76 kg is from the other mechanical components. For the heaviest link, the thigh, the total mass is 2.62 kg, with 1.76 kg of that coming from the knee and ankle actuators. The total mass of the lower leg and foot links is just 0.62 kg. Within the upper leg, the center of mass is close to the hip pitch joint axis, so the rotational inertia of the link is small, compared to its mass. Additionally, since the lower leg is extremely light and the center of mass of the thigh is near the intersection of the hip joints, the inertial properties of the leg do not depend strongly on the leg configuration, making it easier to model and control.

The hip motors are arranged to make the overall hip assembly as compact as possible while maintaining enough range of motion for running and leaping. Fig. 7 shows how the yaw and ab/ad motors are tilted by $-10°$ and $15°$, respectively, which allows the hip pitch joint to achieve the $180°$ of motion shown in Fig. 6. The knee actuator is placed as close as possible to the hip to minimize leg inertia, while also avoiding any interference that would limit the motion of the hip pitch joint.

An important design decision was to move the ankle actuator above the knee joint to reduce the inertia of the lower leg link. As a result, the ankle actuator is located next to the knee actuator on the upper leg link, and a parallel belt
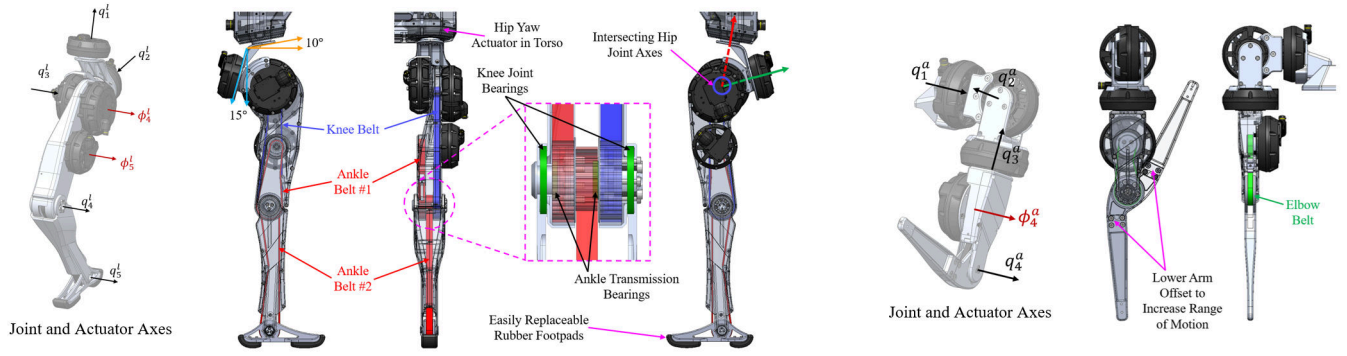
Fig. 7. **Design details for the robot limbs.** Left: Leg joint and actuator axes. Design details involving the hip joint and the internal belt transmission for the left leg. Right: Arm joint and actuator axes. Design details involving the belt transmission and range of motion for the elbow joint of the right arm.

transmission is used to actuate the knee and ankle joints. One belt is used between the knee actuator and the knee joint, while two belts are used for the ankle: the first connects the ankle actuator to a floating set of pulleys on the knee shaft and the second connects the knee shaft pulleys to the ankle joint. Each of the belts is labeled in the left of Fig. 7. Both of the belt transmissions in the upper leg have extra 2:1 reductions to increase the maximum joint torques of the knee and ankle. The increased torque capability of these joints will be required during jumping, leaping, flipping, etc., although it comes at the expense of lowering the maximum joint speeds. We use Gates PolyChain GT Carbon belts, which use carbon fiber tensile members that are approximately 50% stiffer than Kevlar tensile members. This increased stiffness improves the control bandwidth at the knee and ankle joints.

For the knee and ankle joints, the actuator angles, ϕ_i^l, are related to the joint angles, q_i^l, by

$$q_4^l = \phi_4^l; \quad q_5^l = \phi_5^l - \phi_4^l \quad (1)$$

where the subscripts 4 and 5 refer to the knee and ankle angles, respectively, as shown in Fig. 7. The Jacobian for mapping the velocities and torques between the actuator and joint angles, obtained by differentiating (1) with respect to time, is given by

$$\begin{bmatrix} \dot{q}_4^l \\ \dot{q}_5^l \end{bmatrix} = \boldsymbol{J}_p \begin{bmatrix} \dot{\phi}_4^l \\ \dot{\phi}_5^l \end{bmatrix}, \qquad \boldsymbol{J}_p = \begin{bmatrix} 1 & 0 \\ -1 & 1 \end{bmatrix}$$
$$\begin{bmatrix} \tau_4^q \\ \tau_5^q \end{bmatrix} = \boldsymbol{J}_p^{-T} \begin{bmatrix} \tau_4^\phi \\ \tau_5^\phi \end{bmatrix}, \qquad \boldsymbol{J}_p^{-T} = \begin{bmatrix} 1 & 1 \\ 0 & 1 \end{bmatrix} \quad (2)$$

where τ^q and τ^ϕ represent the joint and actuator torques, respectively. We compare the resulting joint torque and speed limits of our parallel actuation design to two alternatives, a serial chain and a differential, in Fig. 8. Fig. 8(c) shows the effective mass belted ellipsoids [23] at the toe and heel of the foot for each type of actuation scheme. Moving the actuator inertia up the leg helps to reduce the effective mass, as the serial chain design has the highest effective mass in almost every direction. For the parallel design, moving the ankle joint does not require moving both rotors, like it would for the differential joint. Additionally, the knee actuator does not move the mass of the ankle motor, like it would for the

serial chain. The downside of the parallel design is that the ankle joint velocity depends on the knee joint velocity and the knee joint torque depends on the ankle joint torque, as seen in the off-diagonal terms of $\boldsymbol{J}_p$ and $\boldsymbol{J}_p^{-T}$ in (2). This is also depicted in the Fig. 8(a) and (b), respectively. The shape of the area of possible torque-speed outputs for the knee and ankle joints is different for the parallel design compared to the serial chain or differential.

While the hip joints can be directly supported by the crossed-roller bearings in the actuators, the knee joint is not collocated with an actuator. So, we use two large diameter, thin section ball bearings to support the joint. The shell structures of the upper and lower legs support the bearings, which are placed as far apart as possible along the knee joint shaft to improve rigidity.

There are three pulleys on the knee shaft for the belt transmissions; these are separated by thin Delrin spacers to keep the belts aligned and reduce belt friction due to rubbing. The two ankle belt pulleys are supported by two internal ball bearings on the knee shaft, while the knee joint output pulley is rigidly attached to the lower leg shell. Finally, there are cutouts in the back side of the upper and lower leg shells to avoid interference with the second ankle belt and increase the range of motion of the knee.

A downside of the placement of the ankle actuator is that it restricts the ankle to one degree of freedom, ankle pitch. Many humanoid robots have a second ankle degree of freedom, ankle roll, which can be achieved by using a second actuator in the foot or by using a differential mechanism in the lower leg. Adding a second ankle actuator above the knee would require two more belts as well as a heavier lower leg, due to the added mechanical structure for the differential, so we have not included the ankle roll degree of freedom in this version of the robot.

We use easily replaceable molded urethane footpads on the toe and heel to soften impacts and provide additional traction during locomotion.

D. Arm Design Details

In this version of the robot, we focused on the leg design, so the arm design is less optimized. Each arm has four degrees of freedom: three in the shoulder and one at the

elbow. The specifications of the arm joints are given in the bottom four rows of Table II, and the joint and actuator axes and other design details are shown in the right of Fig. 7. The elbow actuator is placed on the upper arm link, closer to the shoulder, and uses a belt transmission with a ratio of 1.5:1. Moving the actuator reduces the limb inertia and also physical volume of the elbow joint. The asymmetric design of the lower arm link increases the flexion range of motion of the elbow joint. The forearm is designed to be easily swappable to add hands or grippers to the robot.

IV. ROBOT CONTROL

The mechanical design of the robot enables a model-based control framework to generate and control dynamic motions on the hardware with relatively small sim-to-real gap. Here we present a whole-body control (WBC) framework for pose control and dynamic walking, as well as a nonlinear trajectory optimization framework for vertical jumping.

A. Whole-Body Control

The WBC leverages the full-order dynamics to enable the humanoid to execute various dynamic motions including pose control and walking. The WBC formulation, which follows our previous work [24], is given by

$$\min_{\ddot{\boldsymbol{q}}, \boldsymbol{\tau}, \boldsymbol{u}} \quad \sum_i ||\boldsymbol{A}_i \ddot{\boldsymbol{q}} + \boldsymbol{b}_i||^2_{Q_i} + ||\ddot{\boldsymbol{q}}||^2_{R_{\ddot{q}}} + ||\boldsymbol{\tau}||^2_{R_{\tau}} + ||\boldsymbol{e}_u||^2_{R_u}$$

$$\begin{aligned} \text{s.t.} \quad & \boldsymbol{H}\ddot{\boldsymbol{q}} + \boldsymbol{C} = \boldsymbol{S}_a^\top \boldsymbol{\tau} + \boldsymbol{J}_c^\top \boldsymbol{u}, \\ & \boldsymbol{J}_c \ddot{\boldsymbol{q}} + \dot{\boldsymbol{J}}_c \dot{\boldsymbol{q}} = \boldsymbol{0}, \\ & \boldsymbol{u} \in \mathbb{U}, \\ & |\boldsymbol{\tau}| \le \boldsymbol{\tau}_{max}, \ |\ddot{\boldsymbol{q}}| \le \ddot{\boldsymbol{q}}_{max}, \end{aligned} \tag{3}$$

where $\boldsymbol{A}_i$ is the task Jacobian matrix with task index i; $\boldsymbol{b}_i = \dot{\boldsymbol{A}}_i \dot{\boldsymbol{q}} - \ddot{\boldsymbol{x}}_i$ where $\dot{\boldsymbol{A}}_i$ is the time derivative of $\boldsymbol{A}_i$, and $\ddot{\boldsymbol{x}}$ is the commanded task acceleration; $\boldsymbol{e}_u$ is a term that penalizes deviation from the reference contact force; joint acceleration $\ddot{\boldsymbol{q}} \in \mathbb{R}^n$ and joint torque $\boldsymbol{\tau} \in \mathbb{R}^m$ are regularized through quadratic cost terms in the objective; $\boldsymbol{H} \in \mathbb{R}^{n \times n}$ is the mass matrix; $\boldsymbol{C} \in \mathbb{R}^n$ is the vector that includes the Coriolis, centrifugal, and gravitational forces; $\boldsymbol{S}_a \in \mathbb{R}^{m \times n}$ is the actuation selection matrix; $\boldsymbol{J}_c \in \mathbb{R}^{n_c \times n}$ is the contact Jacobian matrix, where n_c denotes the number of contacts, and $\dot{\boldsymbol{J}}_c$ is the time derivative of $\boldsymbol{J}_c$; $\mathbb{U}$ is the contact wrench cone; $\boldsymbol{\tau}_{max}, \ddot{\boldsymbol{q}}_{max}$ denote the box constraint on the joint torque and acceleration, respectively. In this framework, the torso orientation is represented by roll-pitch-yaw Euler angles, and the angular velocity is given by their time derivatives in the body frame.

1) Tasks: In the context of humanoid walking control, the WBC control tasks include torso pose regulation, swing foot tacking, joint angle and centroidal angular momentum regulation. The desired task acceleration $\ddot{\boldsymbol{x}}_i$ in equation (3) includes both the feedforward and the proportional-derivative (PD) feedback terms

$$\ddot{\boldsymbol{x}}_i = \ddot{\boldsymbol{x}}_i^d + \boldsymbol{K}_p (\boldsymbol{x}_i^d - \boldsymbol{x}_i) + \boldsymbol{K}_d (\dot{\boldsymbol{x}}_i^d - \dot{\boldsymbol{x}}_i) \tag{4}$$

where $\ddot{\boldsymbol{x}}_i, \dot{\boldsymbol{x}}_i, \boldsymbol{x}_i$ are the acceleration, velocity and position, respectively; the superscript $(\cdot)^d$ indicates the desired value;
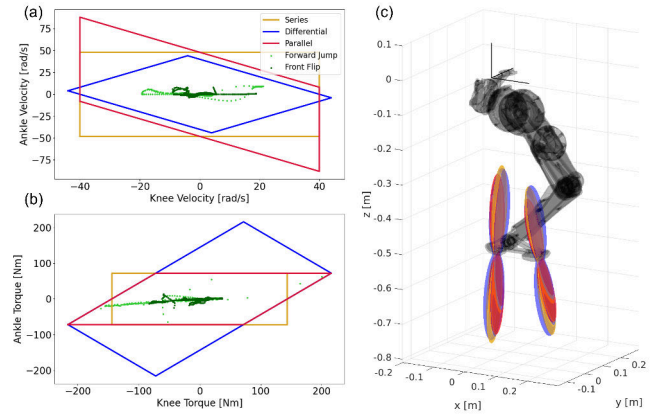

Fig. 8. **Comparing joint actuation schemes.** Using the same pair of U12 and U10 motors, the joint space velocity (a) and torque limits (b) change based on the actuator transmission. For context, two simulated reference motions are also plotted. Depending on the actuation scheme, the effective mass in any direction also changes, for the same leg configuration (c).

$\boldsymbol{K}_{p/d}$ are the proportional/derivative gain matrices. The centroidal angular momentum (CAM) task aims to minimize the total centroidal angular momentum, and takes the form $\dot{\boldsymbol{k}}_G^d = -\boldsymbol{K}_d \boldsymbol{k}_G$.

2) Contact Wrench Cone: Each foot of the MIT Humanoid is modeled as a two-point contact, with one point for the heel and one for the toe. The contact wrench cone at each point is defined by a set of linear inequality constraints

$$\mathbb{U} := \{\boldsymbol{u} \in \mathbb{R}^3 | u_n \le u^{max}, |u_t| \le \mu \cdot u_n\} \tag{5}$$

where the subscripts $(\cdot)_n$ and $(\cdot)_t$ indicate normal and tangential components of the contact force, respectively; μ is the friction coefficient; u^{max} is the maximum normal force.

3) Solving the Quadratic Program: The whole-body control (3) is transcribed to a convex Quadratic Program (QP) problem with 54 variables, which can be efficiently solved using the open-source QP solver qpSWIFT [25] at 500 Hz.

B. Dynamic Jumping Control

Dynamically feasible reference trajectories for vertical jumping are generated via nonlinear trajectory optimization of a planar model of the robot and tracked by a high-frequency tracking controller similar to [19]. The optimization problem is formulated using CasADi [26] in MATLAB and solved using KNITRO [27]. The purpose of the optimization is to find trajectories at the boundary of the robot's capabilities, and the presented approach requires significant tuning to find a feasible local minimum.

The optimization problems seeks to find the optimal state $(\boldsymbol{q}, \dot{\boldsymbol{q}}, \ddot{\boldsymbol{q}})$ and control $(\boldsymbol{\tau}, \boldsymbol{u})$ trajectories that minimize a task specific cost while satisfying the following constraints at each timestep:

1) *Inverse Dynamics*: $\boldsymbol{H}\ddot{\boldsymbol{q}} + \boldsymbol{C} = \boldsymbol{S}_a^\top \boldsymbol{\tau} + \boldsymbol{J}_c^\top \boldsymbol{u}$.
2) *Euler Integration*: $\boldsymbol{q}_{i+1} = \boldsymbol{q}_i + \dot{\boldsymbol{q}}_i \Delta t, \quad \dot{\boldsymbol{q}}_{i+1} = \dot{\boldsymbol{q}}_i + \ddot{\boldsymbol{q}}_i \Delta t$.
3) *Kinematic Feasibility*: Obeying range of motion limits (Table II) and avoiding ground penetration.
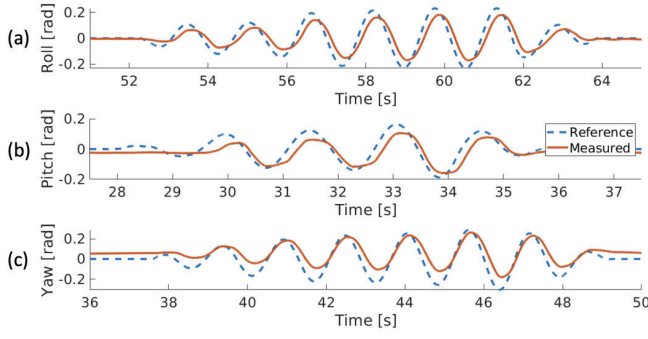4) *Contact Wrench Cone*: A planar version of (5).

Fig. 9. **Pose control tracking performance.** The MIT Humanoid can track sinusoidal orientation reference trajectories with angular velocities up to 6 rad/s in the (a) roll, (b) pitch and (c) yaw directions.
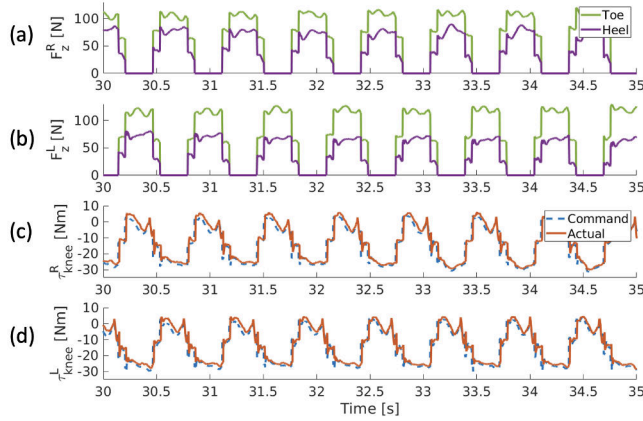

Fig. 10. **Dynamic walking data.** (a) and (b) show the vertical ground reaction force F_z for the right and left legs, respectively. The heel and toe forces are presented in blue and red, respectively. (c) and (d) demonstrate the torque-tracking capability of the lower-level controller. The actual torque (red curve) closely follows the commanded knee joint torque of both legs.

5) *Actuator Constraints*: Motors must respect the torque-speed limits shown in Fig. 5. This involves accounting for the parallel belt transmission of the knee.
6) *Power Limits*: The electrical power consumed by the motors must not exceed the capabilities of the power supply.

All tasks consist of a take-off phase, where the feet (toes and heels) are in contact with the ground, followed by a flight phase, and the durations of these phases are manually pre-determined. For the vertical jump, the task-specific cost is simply to maximize the terminal height of the center of mass while maintaining an upright posture. This framework does not consider the landing phase of the jump.

V. HARDWARE EXPERIMENTS

A. Pose Control

The combination of high control bandwidth actuators and the WBC framework (3) enables the MIT Humanoid to track fast reference motions. In this experiment, the robot is commanded to track sinusoidal orientation trajectories with an angular velocity of 6 rad/s. As shown in Fig. 9, the MIT Humanoid can track the fast reference in the roll, pitch and yaw directions while maintaining balance by leveraging the full-order dynamics.
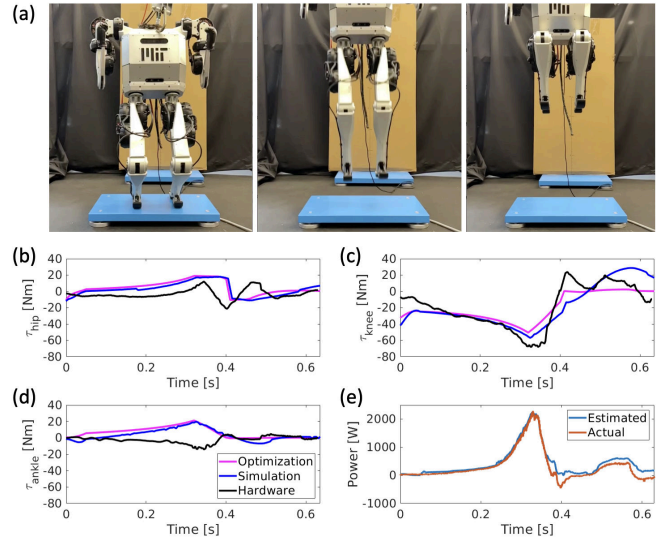

Fig. 11. **Vertical jumping performance.** (a) Pictures of the robot performing a 30 cm vertical jump, as measured by the torso displacement (50 cm at the feet). (b),(c),(d) Comparing torques between the optimization output, simulation tests, and hardware tests, for the hip, knee and ankle respectively. (e) Estimated power required from simulation vs. the actual recorded power for the jump.

B. Walking

In this experiment, the torso is commanded to track a centroidal trajectory while a phase-based gait schedule determines the transition between the stance phase and swing phase for each leg. The swing leg tracks a prescribed polynomial trajectory whose endpoint is the next desired footstep location.

Fig. 10 shows the data from the dynamic walking experiment. The gait period is 650 ms and the stance duration is 390 ms, which results in a 65 ms double stance phase. The vertical ground reaction forces at the heel and toe in Fig. 10(a) and (b) show each leg alternating among the swing, double stance and single stance phases. Since the robot's desired center of mass height is constant, the total vertical forces at any moment of time sums to roughly the total weight of the robot.

One of the key features of the proprioceptive actuators used in the MIT Humanoid is the high-fidelity torque tracking capability. Fig. 10(c) and (d) show the knee torque tracking performance of the low-level impedance controller. The knee torque is representative of the other joint torques, as the knee requires the highest maximum torque during walking.

C. Vertical Jumping

Following reference jumping trajectories generated using the optimization presented in Section IV, the robot was able to perform a vertical jump of approximately 30 cm, measured by estimating the torso displacement, with the feet clearing a height of 50 cm. The jump height was calculated as the difference in the height of the robot's torso between takeoff and apex of the jump. It was measured using a ruled surface in the background of the video experiments. The jump height of 30 cm is approximately 29% of the robot's

height, compared to 18% [14] and 20% [28] from previous jumping experiments performed on humanoid robots. Fig. 11 shows still frames of the robot during a vertical jump along with plots of the joint torques and the electrical power into the system. Since the optimization framework does not produce a landing controller, we let the robot land in a soft joint PD control mode. As the robot does not control its landing pose, this data is not shown in the plot. These jumping results begin to push the dynamic capabilities of the system, reaching peak electrical power values of roughly 2.1 kW. Our lack of an accurate state estimator for flight and landing prevented us from achieving stable landing of the demonstrated jumps. However, the ability of the robot to endure ground impacts after each jump without a robust landing controller further demonstrates it durability. These results begin to show the capabilities of the system but are far from the torque and power limits of the actuators. With more focus on the optimization pipeline, system modelling, and landing controllers, this platform will be capable of even the most demanding of dynamic tasks.

VI. Conclusion

In this work, we have presented the design of the MIT Humanoid robot platform. The robot's high-fidelity torque tracking ability plays a crucial role in the successful control of the robot, as demonstrated by our balancing and walking experiments. The proprioceptive actuation also allows the robot to execute dynamic and high-power motions, as demonstrated by our vertical jumping experiments.

Our long-term goal for the robot is performing seamless combinations of high-speed running and leaping maneuvers, similar to parkour athletes. Based on the early experiments presented here, we are confident the MIT Humanoid platform will be able to achieve these behaviors.

References

[1] *Atlas*, https://www.bostondynamics.com/atlas, Boston Dynamics, 2023.

[2] M. Chignoli, D. Kim, E. Stanger-Jones, and S. Kim, "The mit humanoid robot: Design, motion planning, and control for acrobatic behaviors," in *IEEE-RAS 20th International Conference on Humanoid Robots (Humanoids)*, 2021.

[3] S. Seok, A. Wang, M. Y. Chuah, *et al.*, "Design principles for energy-efficient legged locomotion and implementation on the mit cheetah robot," *IEEE/ASME Transactions on Mechatronics*, 2015.

[4] P. M. Wensing, A. Wang, S. Seok, D. Otten, J. Lang, and S. Kim, "Proprioceptive actuator design in the mit cheetah: Impact mitigation and high-bandwidth physical interaction for dynamic legged robots," *IEEE Transactions on Robotics*, 2017.

[5] B. Katz, J. Di Carlo, and S. Kim, "Mini cheetah: A platform for pushing the limits of dynamic quadruped control," in *IEEE International Conference on Robotics and Automation (ICRA)*, 2019.

[6] M. H. Raibert, *Legged robots that balance*. MIT press, 1986.

[7] *Asimo*, https://global.honda/innovation/robotics/ASIMO.html, Honda, 2011.

[8] J. Englsberger, A. Werner, C. Ott, *et al.*, "Overview of the torque-controlled humanoid robot toro," in *IEEE-RAS International Conference on Humanoid Robots (Humanoids)*, 2014.

[9] P. Seiwald, S.-C. Wu, F. Sygulla, *et al.*, "Lola v1. 1– an upgrade in hardware and software design for dynamic multi-contact locomotion," in *IEEE-RAS 20th International Conference on Humanoid Robots (Humanoids)*, 2021.

[10] S. Lohmeier, T. Buschmann, and H. Ulbrich, "Humanoid robot lola," in *IEEE International Conference on Robotics and Automation (ICRA)*, 2009.

[11] J. Lim, I. Lee, I. Shim, *et al.*, "Robot system of drc-hubo+ and control strategy of team kaist in darpa robotics challenge finals," *Journal of Field Robotics*, 2017.

[12] C. Hubicki, J. Grimes, M. Jones, *et al.*, "Atrias: Design and validation of a tether-free 3d-capable spring-mass bipedal robot," *The International Journal of Robotics Research*, 2016.

[13] *Agility robotics*, https://agilityrobotics.com/robots, Agility Robotics, 2016.

[14] K. Kojima, Y. Kojio, T. Ishikawa, *et al.*, "Drive-train design in jaxon3-p and realization of jump motions: Impact mitigation and force control performance for dynamic motions," in *IEEE/RSJ International Conference on Intelligent Robots and Systems (IROS)*, 2020.

[15] D. Crowley, J. Dao, H. Duan, K. Green, J. Hurst, and A. Fern, "Optimizing bipedal locomotion for the 100m dash with comparison to human running," in *IEEE International Conference on Robotics and Automation (ICRA)*, 2023.

[16] *Nadia*, https://boardwalkrobotics.com/Nadia.html, Boardwalk Robotics, 2023.

[17] Y. Ding, A. Pandala, C. Li, Y.-H. Shin, and H.-W. Park, "Representation-free model predictive control for dynamic motions in quadrupeds," *IEEE Transactions on Robotics*, 2021.

[18] G. Bledt, M. J. Powell, B. Katz, J. Di Carlo, P. M. Wensing, and S. Kim, "Mit cheetah 3: Design and control of a robust, dynamic quadruped robot," in *IEEE/RSJ International Conference on Intelligent Robots and Systems (IROS)*, 2018.

[19] Q. Nguyen, M. J. Powell, B. Katz, J. Di Carlo, and S. Kim, "Optimized jumping on the mit cheetah 3 robot," in *IEEE International Conference on Robotics and Automation (ICRA)*, 2019.

[20] Y. Sim and J. Ramos, "Tello leg: The study of design principles and metrics for dynamic humanoid robots," *IEEE Robotics and Automation Letters*, 2022.

[21] *Kangaroo*, https://pal-robotics.com/robots/kangaroo/, PAL Robotics, 2023.

[22] T. Zhu, "Design of a highly dynamic humanoid robot," Ph.D. dissertation, 2023.

[23] O. Khatib, "Inertial properties in robotic manipulation: An object-level framework," *The international journal of robotics research*, 1995.

[24] Y. Ding, C. Khazoom, M. Chignoli, and S. Kim, "Orientation-aware model predictive control with footstep adaptation for dynamic humanoid walking," in *IEEE-RAS 21st International Conference on Humanoid Robots (Humanoids)*, 2022.

[25] A. G. Pandala, Y. Ding, and H.-W. Park, "Qpswift: A real-time sparse quadratic program solver for robotic applications," *IEEE Robotics and Automation Letters*, 2019.

[26] J. A. Andersson, J. Gillis, G. Horn, J. B. Rawlings, and M. Diehl, "Casadi: A software framework for nonlinear optimization and optimal control," *Mathematical Programming Computation*, 2019.

[27] R. H. Byrd, J. Nocedal, and R. A. Waltz, "K nitro: An integrated package for nonlinear optimization," *Large-scale nonlinear optimization*, 2006.

[28] H. Qi, X. Chen, Z. Yu, *et al.*, "Vertical jump of a humanoid robot with cop-guided angular momentum control and impact absorption," *IEEE Transactions on Robotics*, 2023.